Correlating nuclear morphology and external force with combined atomic force microscopy and light sheet imaging separates roles of chromatin and lamin A/C in nuclear mechanics

Chad M. Hobson[a,*], Megan Kern[a], E. Timothy O'Brien III[a], Andrew D. Stephens[b], Michael R. Falvo[a], and Richard Superfine[c,*]

[a]Department of Physics and Astronomy and [c]Department of Applied Physical Sciences, The University of North Carolina at Chapel Hill, Chapel Hill, NC 27599; [b]Biology Department, The University of Massachusetts at Amherst, Amherst, MA 01003, The University of North Carolina at Chapel Hill, Chapel Hill, NC 27599

ABSTRACT **Nuclei are often under external stress, be it during migration through tight constrictions or compressive pressure by the actin cap, and the mechanical properties of nuclei govern their subsequent deformations. Both altered mechanical properties of nuclei and abnormal nuclear morphologies are hallmarks of a variety of disease states. Little work, however, has been done to link specific changes in nuclear shape to external forces. Here, we utilize a combined atomic force microscope and light sheet microscope to show SKOV3 nuclei exhibit a two-regime force response that correlates with changes in nuclear volume and surface area, allowing us to develop an empirical model of nuclear deformation. Our technique further decouples the roles of chromatin and lamin A/C in compression, showing they separately resist changes in nuclear volume and surface area, respectively; this insight was not previously accessible by Hertzian analysis. A two-material finite element model supports our conclusions. We also observed that chromatin decompaction leads to lower nuclear curvature under compression, which is important for maintaining nuclear compartmentalization and function. The demonstrated link between specific types of nuclear morphological change and applied force will allow researchers to better understand the stress on nuclei throughout various biological processes.**

Monitoring Editor
Dennis Discher
University of Pennsylvania

Received: Jan 28, 2020
Revised: Mar 23, 2020
Accepted: Mar 31, 2020

INTRODUCTION

The nucleus, which encapsulates and protects the entire genome, functions not only as the site of gene replication and transcription, but also as a fundamental mechanical constituent of the cell. Altered nuclear mechanics and nuclear morphology have both been linked to various disease states ranging from Hutchinson-Gilford Progeria Syndrome (De Sandre-Giovannoli *et al.*, 2003; Dahl *et al.*, 2006; Butin-Israeli *et al.*, 2012) and Emery-Dreifuss muscular dystrophy (Lammerding *et al.*, 2004, 2005; Butin-Israeli *et al.*, 2012) to breast cancer (Butin-Israeli *et al.*, 2012; Tocco *et al.*, 2018). Such diseased cells are often under stress either through external means such as cellular migration (Davidson *et al.*, 2014; Harada *et al.*, 2014) or intracellular forces like that of actin prestress (Lammerding and Wolf, 2016), which has been shown to be sufficient to cause nuclear rupture (Hatch and Hetzer, 2016; Lammerding and Wolf, 2016). Little work, however, has studied either the dynamic relationship between external forces and nuclear morphology or the role of nuclear mechanical constituents in this relationship. To fully understand the complex connections linking nuclear mechanics and morphology with disease and cellular function, we must first understand the intermediate relationship of how nuclear mechanical constituents resist external forces to maintain morphology.

Nuclear mechanics are primarily dictated by the nuclear lamina and chromatin, as well as indirectly influenced by the cytoskeleton

This article was published online ahead of print in MBoC in Press (http://www.molbiolcell.org/cgi/doi/10.1091/mbc.E20-01-0073) on April 8, 2020.

*Address correspondence to: Chad M. Hobson (hobsonc@live.unc.edu); Richard Superfine (superfine@unc.edu)

Abbreviations used: AFM, atomic force microscopy; AFM-LS, combined atomic force microscopy and light sheet imaging system; FEA, finite element analysis; LA/C KD, lamin A/C knock down; NCSA, nuclear cross-sectional area; NP, nuclear perimeter; TSA, trichostatin A; WT, wild type.

(Stephens *et al.*, 2019). The cytoskeleton protects the nucleus both through an actin cap (Khatau *et al.* 2009; Haase *et al.* 2016; Kim *et al.* 2018) and a perinuclear cage of the intermediate filament vimentin (Neelam *et al.*, 2015; Patteson *et al.*, 2019; Rosso *et al.*, 2019). The nuclear lamina, primarily lamin A/C, has consistently been shown to be a major mechanical constituent of the nucleus through constricted migration, micropipette aspiration, AFM, micromanipulation, and other techniques (Dahl *et al.*, 2004, 2005; Lammerding *et al.*, 2004, 2006; Lee *et al.*, 2007; Pajerowski *et al.*, 2007; Schape *et al.*, 2009; Swift *et al.*, 2013; Hanson *et al.*, 2015; Neelam *et al.*, 2015; Stephens *et al.*, 2017). Furthermore, the understanding of chromatin's role as a mechanical element of the nucleus continues to be refined. Through examining swollen *Xenopus* oocyte nuclei, it was first thought that chromatin had little role in the mechanical properties of nuclei (Dahl *et al.*, 2004). Additional work, however, revealed that chromatin indeed does contribute to nuclear stiffness, and that (de)compaction of chromatin leads to nuclear (softening) stiffening (Dahl *et al.*, 2005; Pajerowski *et al.*, 2007; Mazumder *et al.*, 2008; Krause *et al.*, 2013; Erdel et al., 2015; Schreiner *et al.*, 2015; Shimamoto *et al.*, 2017; Stephens *et al.*, 2017, 2018; Neubert *et al.*, 2018). The specific roles of chromatin and lamin A/C in nuclear mechanics have begun to be disentangled, as micromanipulation experiments have shown that chromatin dominates small extensions while lamin A/C dominates large extensions (Stephens *et al.*, 2017). Both the mechanical constituents of the nucleus—the nuclear lamina and chromatin—as well as the cytoskeleton are paramount for protection of the genome and subsequently cellular function.

Directly related to the mechanical properties of nuclei is nuclear morphology; this is in general characterized by nuclear volume and nuclear surface area, or the more experimentally accessible 2D surrogates of nuclear cross-sectional area (*NCSA*) and nuclear perimeter (*NP*), respectively, as well as local curvature. Nuclear morphology also relates to nuclear abnormalities and/or blebs displayed across the spectrum of human disease (Stephens *et al.*, 2019). However, here we are primarily concerned with morphology in regard to general nuclear shape. A variety of metrics have been used to quantify changes in nuclear morphology, such as area strain (percent change in projected cross-sectional area; Zhang *et al.*, 2019) and 3D irregularity (ratio of excess volume of a fitted convex hull to nuclear volume; Tocco *et al.*, 2018). Aside from the previously noted connections to disease, nuclear morphology has further been linked to levels of transcriptional activity as nuclei with reduced volume enter a more quiescent state (Damodaran *et al.*, 2018). Increases in the volume of nuclei either through swelling (Finan *et al.*, 2011) or directed migration on patterned substrates (Katiyar *et al.*, 2019) has been shown to decondense or dilate chromatin levels. Stretching of the nuclear surface area is thought to be a mechanism of nuclear mechanotransduction (Enyedi and Niethammer, 2017; Donnaloja *et al.*, 2019). Nuclear morphology is also characterized in part by local curvature; regions of high local curvature have been linked to nuclear rupture (Xia *et al.*, 2018) and nuclear blebs (Stephens *et al.*, 2018; Cho *et al.*, 2019). Nuclear morphology is directly related to both the mechanical integrity of the nucleus as well as nuclear and cellular function.

Previous work has used changes in nuclear morphology under force application as a metric for mechanical resistance (Neelam *et al.*, 2015; Haase *et al.*, 2016); that is, smaller changes in nuclear morphology imply a stiffer nucleus. Nuclear morphology has also been used in studying stored elastic energy (Tocco *et al.*, 2018) and pressure gradients (Finan *et al.*, 2009; Kim *et al.*, 2015). Investigators have further developed an analytical model connecting nuclear morphology to external forces and mechanical properties for an idealized geometry (Balakrishnan *et al.*, 2019). However, a majority of work regarding nuclear mechanics is either agnostic to nuclear shape or focuses on a highly specific model of a single technique. For example of the former, atomic force microscopy (AFM) studies of nuclei have traditionally used a Hertzian contact mechanics model, which models the nucleus as a linearly elastic, isotropic, homogeneous material under small indentation (Johnson, 1985). Previous work, however, has shown the nucleus to be both nonlinear (Stephens *et al.,* 2017) and anisotropic (Haase *et al.*, 2016). While Hertzian analysis has brought to light many novel insights, it is limited by its ability to decouple contributions of specific structures. More intricate computational models have given direct insight into many mechanical techniques, including constricted migration (Cao *et al.*, 2016), micropipette aspiration (Vaziri and Mofrad, 2007), magnetic bead twisting (Karcher *et al.*, 2003), plate compression (Caille *et al.*, 2002), micromanipulation (Banigan *et al.*, 2017; Stephens *et al.*, 2017), and AFM (Lherbette *et al.*, 2017); however, their specificity inhibits extrapolation of their conclusions. There exists a need for an intermediate understanding of nuclear deformation that informs both the relative contributions of the various nuclear mechanical constituents as well as their roles in protecting against specific deformations to nuclear morphology.

In this work, we address some of these open questions regarding the links between mechanics and morphology through the use of our combined atomic force microscope and side-view light sheet microscope (AFM-LS; Nelsen *et al.*, 2019). Our approach allows us to visualize cells from the side (*x-z* cross-section) with high spatiotemporal resolution during compression with an atomic force microscope. We use this technique to correlate changes in apparent SKOV3 nuclear volume and nuclear surface area with applied force to develop an empirical model for nuclear deformation, which has applications for assays beyond our own technique and is applicable to nonstandard nuclear shapes. This allows us to disentangle the contributions of chromatin and lamin A/C to strain in nuclear volume and nuclear surface area, respectively, an insight not possible with previous AFM models and techniques. We also measure the dynamics of nuclear curvature under compression, and show that chromatin decompaction reduces curvature at the site of indentation; this indirectly shows the nucleus behaves as a two-material system. To further interpret our findings, we develop a finite element analysis (FEA) model—allowing us to computationally study nuclear deformation for discretized, nonstandard nuclear geometries—that recapitulates our empirical results and connects them to material properties. In summary, we provide the first decoupling of the role of chromatin and lamin A/C in nuclear compression as well as a new insight into the connection between external forces, nuclear mechanical constituents, and nuclear shape and curvature.

RESULTS

Combined AFM and side-view light sheet microscopy show strain in nuclear volume and surface area begin at different indentations

Our combined atomic force microscope and side-view light sheet fluorescence microscope (Figure 1A) allows visualization of the dynamics of cellular deformations in the plane of applied force while simultaneously monitoring the force response of the cell (Nelsen *et al.*, 2019). We have previously used this tool to show the existence of separate elastic moduli correlated with whole-cell and nuclear deformations (Beicker *et al.*, 2018). We built on this previous work by studying the dynamics of nuclear morphology and the correlated force response under compression by AFM. We examined a time

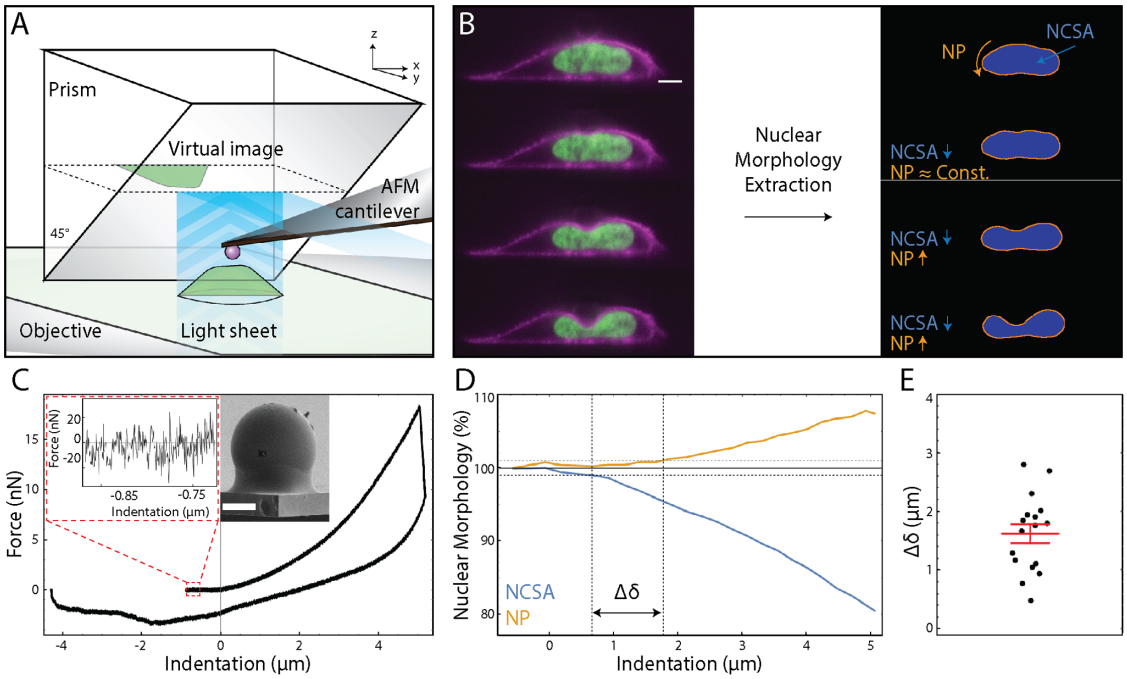

FIGURE 1: Combined atomic force microscopy and side-view light sheet microscopy (AFM-LS) extracts dynamics of nuclear morphology and applied force under whole-cell compression. (A) Cartoon schematic of our AFM-LS system. A full description is provided in our previous work. (B) A subset of fluorescence images collected by our AFM-LS during indentation of a live, SKOV3 cell (scale bar = 5 μm). The cell is stably expressing snap-tagged KRas-tail (magenta) and Halo-tagged H2B (green) labeled with Janelia Fluor 503 and 549, respectively. Custom workflow (see *Materials and Methods*) allows for extraction of nuclear perimeter (*NP*) and nuclear cross-sectinoal area (*NCSA*). (C) Force vs. indentation data for the previously displayed compression experiment. Left inset provides a scale for the noise in the force data. Right inset shows a scanning electron microscope image of a bead glued to the end of an AFM cantilever (see *Materials and Methods*). Beads are nominally 6 μm in diameter; this bead was measured to be 5.4 μm in diameter (scale bar = 2 μm). (D) Nuclear morhpology as a percentage vs. indentation for the previously displayed compression experiment. Orange and blue represent *NP* and *NCSA*, respectively. $\Delta\delta$ is defined to be the difference in indentation at which *NP* and *NCSA* reach 1% change. (E) $\Delta\delta$ for $n = 17$ separate compression experiments. The red bar represents the standard error in the mean.

series of side-view images of compressed, live SKOV3 cells stably expressing Halo-tagged histone 2B (H2B, green) and SNAP-tagged K-Ras-tail (magenta) labeled with Janelia Fluor 549 and 503, respectively (Figure 1B and Supplemental Movie 1). Masks of nuclei were generated (see *Materials and Methods*) and used to extract both *NCSA* (blue) and apparent nuclear *NP* (orange) as a function of indentation (Figure 1B). As in prior studies, we used *NCSA* and *NP* as surrogates for nuclear volume and nuclear surface area, respectively, as the qualitative deformation of the nucleus is the same in any side-view orientation (Finan *et al.*, 2011). The AFM provided synchronized force data with approximately 20 pN resolution during the side-view image acquisition (Figure 1C and Supplemental Movie 1). It should be noted that our measurements of apparent nuclear perimeter are not necessarily the same as measuring the perimeter of the nuclear envelope. The nucleus is not a closed system in general; the outer nuclear membrane is contiguous with the endoplasmic reticulum (Mattaj, 2004) and therefore could add length upon indentation. Furthermore, the nuclear envelope could have undulations that are smoothed out upon compression, similar to previously reported results (Buxboim *et al.*, 2017; Chu *et al.*, 2017). Our analysis of nuclear shape is then more aligned with the shape of the contents of the inner nuclear membrane; that is, primarily the nuclear lamina and the chromatin, which are the primary mechanical constituents of the nucleus. However, previously reported results show in micropipette aspiration studies that strain occurs in both the nuclear lamina in human embryonic stem cells (Pajerowski *et al.*, 2007) and the nuclear envelope in *Xenopus* oocyte nuclei (Dahl *et al.*, 2004).

We first observed that *NCSA* and *NP* underwent strain at different levels of indentation (Figure 1D). We determined this difference in the onset of *NCSA* strain and *NP* strain by linearly interpolating the *NCSA* and *NP* indentation series and computing the difference in indentations at which *NCSA* and *NP* reached 1% strain, denoted by $\Delta\delta$. This was chosen because 1% strain is a point reached in all data sets used in analysis and is far enough above the noise of the nuclear morphology data to confidently indicate a change. The onset of strain in NCSA and *NP* differ by $\Delta\delta = 1.6 \pm 0.7$ μm (mean ± SD of indentation), which is clearly greater than zero. This indicates the presence of two distinct and separate regimes for strain onset of nuclear surface area and nuclear volume (Figure 1E). Moreover, this implies that the apparent nuclear surface area to volume ratio does not follow one simple scaling relationship under AFM compression. Whether the outer nuclear membrane itself is adding length, smoothing out undulations, or physically stretching, however, is not distinguished.

A two-regime force response allows for determination of scaling relationships between nuclear morphology and applied force

Previous research has shown both a two-regime force response upon stretching nuclei with flexible micropipettes (Stephens *et al.*, 2017) as well as the necessity of a term accounting for the stretching

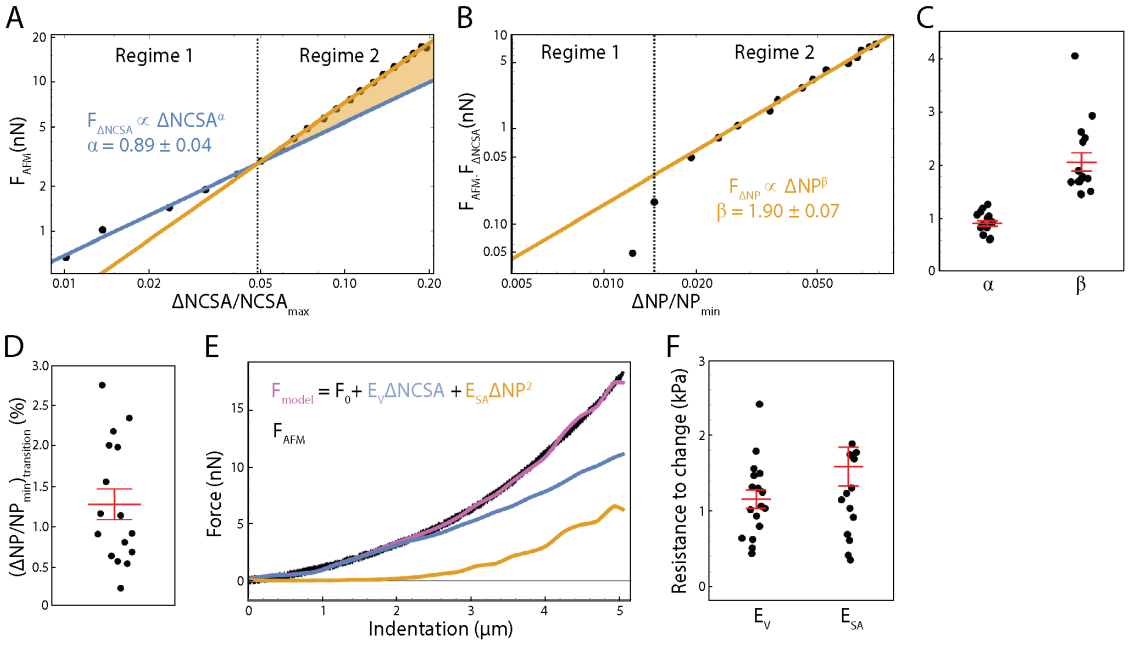

FIGURE 2: Correlating nuclear morphology and applied force informs an emperical model for strain-stiffening response. (A) Force as recorded by the AFM vs. change in *NCSA* plotted on a log-log scale. Two distinct power-law regimes are observed. (B) Force as recorded by the AFM minus the force response in regime 1 plotted against change in *NP* on a log-log scale, showing a single power-law relationship in regime 2. (C) α, the exponent for $F_{\Delta NCSA}$, and β, the exponent for $F_{\Delta NP}$, as determined for $n = 16$ cells. Red bars represent mean and SEM. (D) The strain in *NP* at the transition point between regime 1 and regime 2 as determined for $n = 16$ cells. Red bars represent mean and SEM. (E) An emperical model for nuclear deformation as shown over force vs. indentation. We display our full emperical model (magenta), the individual contributions required to deform the nuclear volume and surface area (blue and orange, respectively), and the AFM data over the full indentaiton. (F) Resistance to nuclear volume change, E_V, and resistance to nuclear surface area change, E_{SA}, as determined for $n = 17$ cells. Red bars represent mean and SEM.

of nuclear surface area to explain nonlinear osmolarity of the nucleus (Finan *et al.*, 2009). This work and our results showing distinct indentation thresholds for nuclear volume and surface area strain led us to hypothesize the existence of a two-regime force response resulting from separate forces associated with changes in nuclear volume and nuclear surface area.

To test this hypothesis, we first examined the scaling relationship between applied force from the AFM, F_{AFM}, and Δ*NCSA* ($NCSA_{Max}$–*NCSA*); note that Δ*NCSA* is positive for a decrease in *NCSA*. We observed a clear, two-regime force response wherein applied force scales with Δ*NCSA* to different powers in each regime (Figure 2A). This phenomenon was seen in all but one cell examined ($n = 17$ cells examined total). To determine the scaling relationships between external force and Δ*NCSA*, we fit two separate power-law relationships between force and Δ*NCSA*—one before and one after the transition point. The transition point between fitting regimes was allowed to vary to minimize error in the power- law fits in both regimes. The exact transition point was determined to be the point at which the two power-law relationships intersect.

Knowing that at small indentations we only observed strain in *NCSA* (constant nuclear surface area) indicates that regime 1 immediately provided us a scaling relationship between external force and Δ*NCSA*. That is, we defined a force associated with Δ*NCSA* given by $F_{\Delta NCSA} \propto \Delta NCSA^{\alpha}$ (blue line, Figure 2A). Under the assumption that the aforementioned relationship was unchanged during indentation, we subtracted $F_{\Delta NCSA}$ from F_{AFM} to isolate the additional force response resulting from strain in *NP* (yellow shaded region, Figure 2A). We then plotted this additional force response against Δ*NP* ($NP - NP_{Min}$) where we observed a constant power-law relationship in regime 2 (yellow line, Figure 2B). We then defined a separate force required to stretch the nuclear surface area given by $F_{\Delta NP} \propto \Delta NP^{\beta}$. Performing this analysis on $n = 16$ cells allowed us to determine that $\alpha = 0.9 \pm 0.2$ and $\beta = 2.1 \pm 0.7$ (mean ± SD; Figure 2C).

Previous work, however, has modeled the nucleus as having a strain-dependent elastic modulus (Lherbette *et al.*, 2017), which could provide an alternate explanation of the origin of the two-regime phenomenon we have observed. To differentiate the two explanations, we examined the transition point as a function of Δ*NP*. The transition point between the two regimes corresponded to 1.2% ± 0.8% (mean ± SD) change in *NP* (Figure 2D), meaning the force response in regime 1 correlated only with strain in *NCSA* while the force response in regime 2 correlated with both strain in *NCSA* and *NP*. This correlation between the onset of regime 2 and the onset of strain in Δ*NP* provided support to our hypothesis that the two regimes are a result of separate forces required to deform the volume and surface area of the nucleus. With the combination of this result and our determination of the specific scaling relationships between applied force and both Δ*NCSA* and Δ*NP*, we then posed the following empirically determined model to correlate nuclear deformation with applied force.

$$F = F_0 + E_V(\Delta NCSA) + E_{SA}(\Delta NP)^2 \quad (1)$$

Here, F_0 represents any force response accumulated before deformation of the nucleus. Our interpretation is that F_0 is a result of compressing the space between the plasma membrane and the nuclear membrane, comprised of the cytosol and cytoskeleton. E_V and E_{SA} are the effective mechanical resistance the cell provides to

changes in nuclear volume and nuclear surface area, respectively, as represented by *NCSA* and *NP*. These resistances are composed of contributions from not only the nucleus, but also from the cytosol, internal pressure gradients, the cytoskeleton, the actin cortex, and other cellular structures. However, the nucleus has been shown to be the stiffest subcellular structure and also encompasses a majority of the strain during compression, implying that E_V and E_{SA} are primarily dictated by the mechanical properties of the nucleus. Our results are consistent in that F_0 is on the order of 100 pN, implying there is minimal force response before deformation of the nucleus. They also inherently include viscous contributions as there is no time scale built directly into our model and our AFM measurements are not fully quasistatic (Supplemental Figure S1). Indenting at higher (lower) rates would then increase (decrease) our measured values of E_V and E_{SA}. While not studied here, this decomposition provides the opportunity to study the relative viscous contributions associated with strain in *NCSA* and *NP*. A single value of E_V and E_{SA} is determined by fitting Eq. 1 to the entire indentation of each cell (Figure 2, E and F). Furthermore, this model and observed two-regime force response holds true for nuclei lacking pretension, as determined by performing the same experiment on more rounded cells induced by a reduction of adhesion to the substrate (Supplemental Figure S2).

We find that for SKOV3 cells, E_{SA} is approximately 1.36 times greater than E_V, implying these nuclei are more susceptible to strain in volume than in surface area. This can be compared with the Hertz model (Johnson, 1985) and the height-corrected Hertz model (Dimitriadis *et al.*, 2002), both of which fail to model the force response over the entirety of the indentation (Supplemental Figure S3). It is also important to note that Hertzian analysis specifies probe and target geometries, and assumes homogeneity and linearity. Our approach, however, makes no prior assumption regarding such geometries and is simply empirical. Moreover, Hertzian analysis is restricted to small indentations as the approximation of contact area breaks down at high strain. Accounting for the eventual plateau of contact area leads to a linear force-indentation relationship, which further underestimates the true force response. Our technique, however, moves beyond this limitation as we make no specific model of contact area and instead examine the empirically determined scaling relationships between shape and force. Our model was constructed across small and large indentations, and is therefore applicable in both scenarios. Our approach also allows us to decouple resistances to specific types of nuclear strain as opposed to providing a single metric of stiffness for the entirety of the nucleus. This complements and improves on earlier analytic modeling efforts (Balakrishnan *et al.*, 2019) in that we have empirically determined a relationship between force and morphology that accounts for contributions of both the bulk compressibility and surface tension without assuming a predefined geometry.

A further alternative model is a polynomial in indentation ($F_{AFM} = a + b\delta + c\delta^n$) that has been reported to fit AFM indentation of the simple red blood cell when adherent (Sen *et al.*, 2005). Here, the linear term is representative of the membrane tension and the higher order term ($n \approx 2$–3) reflects membrane dilation. This work also observed a strain-stiffening effect; however, this stiffening occurs at forces of order 100 pN and indentations of order 100 nm. We also observe similar stiffening at low forces (Supplemental Figure S4), along with an additional stiffening at forces of order 1 nN and indentations of order 1 μm (Figure 2A and Supplemental Figure S4). Our work focuses exclusively on the latter stiffening effect seen at higher forces, for which this alternative approach does not explain. Our scaling relationships for the low-force stiffening do not precisely match that of this alternative mode, but this may be explained by their use of conical AFM tips as compared with our spherical AFM tips. A full model of AFM indentation may then first apply this polynomial approach at quite small forces and indentations, and our empirical approach at large forces and indentations.

Empirical model of nuclear deformation is independent of initial nuclear size

Our AFM-LS technique does not systematically examine a specifically oriented vertical slice as the distribution of polarity among the cells is seemingly random. One potential failure of the proposed model and technique would be a dependence of E_V and E_{SA} on the initial morphology of the nucleus or the orientation in which we image the nucleus from the side. To examine this, we determined both E_{NCSA} and E_{NP} for $n = 17$ cells and plotted E_V and E_{SA} against initial values of *NCSA* and *NP* (Supplemental Figure S5). We performed a Pearson's correlation test between E_V, E_{SA} and *NCSA*, *NP*. No significant correlation was observed between either E_V or E_{SA} and *NCSA* or *NP*, implying that the resistances to nuclear morphology changes determined by our model are not systematically dependent on either the scale of the nucleus or the specific side-view orientation in which we visualized the nucleus. Our approach is then robust to initial cell orientation or initial nuclear size.

Chromatin and lamin A/C separately resist nuclear volume and surface deformations, respectively

Chromatin and lamin A/C have been shown to be the primary mechanical constituents of nuclei; recent work has shown that during micromanipulation extension of isolated nuclei chromatin dominates small-scale extensions while lamin A/C governs large-scale extensions (Stephens *et al.*, 2017). It remains untested whether similar phenomena hold true for compression-based deformations of nuclei in intact cells. We hypothesized that in AFM indentations, chromatin in part dictates the resistance to nuclear volume change while lamin A/C separately resists changes in nuclear surface area. Such a measurement was not previously attainable without AFM-LS.

To test this hypothesis, we first treated our SKOV3 cells with a 200 nM concentration of trichostatin A (TSA) for 24 h before performing AFM compression with side-view imaging experiments. TSA decompacts chromatin by increasing euchromatin marker histone tail acetylation (Supplemental Figure S6; Toth *et al.*, 2004). We extracted nuclear morphology dynamics under compression and fit Eq. 1 to the corresponding force data to extract E_V and E_{SA}. We observed a significant 40% decrease in E_V upon TSA treatment ($p < 0.05$ from a *t* test), but no significant difference in E_{SA} (Figure 3, A and B).

Furthermore, we transfected our SKOV3 cell line with siRNA to halt production of new lamin A/C (LA/C KD; Supplemental Figure S7). We then performed AFM-LS experiments 4–6 d post transfection and extracted E_V and E_{SA} as previously described. We observed a significant 50% decrease in E_{SA} ($p < 0.05$ for a *t* test), yet no significant change in E_V (Figure 3, A and B). This means that chromatin resists strain in nuclear volume while lamin A/C separately resist strain in surface area. Furthermore, this indicates that chromatin does not resist nuclear surface area stretching nor does lamin A/C resist deformation in nuclear volume. Because strain in nuclear volume and nuclear surface area occur at different indentation scales (Figure 1), we have also shown that chromatin and lamin A/C provide mechanical resistance at short and long indentations, respectively.

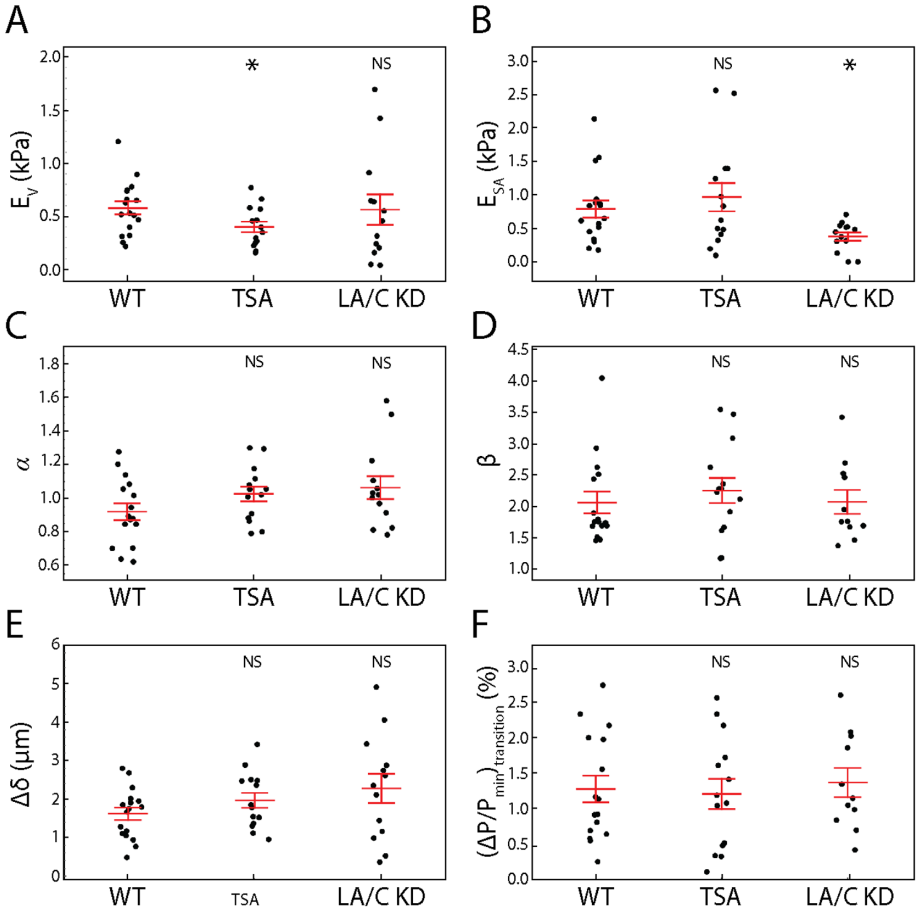

FIGURE 3: Chromatin decompaction and lamin A/C depletion weaken resistance to volume and surface area changes, respectively, while behaving similarly to the empirical model. (A) Resistance to nuclear volume change, E_V, is decreased by TSA but unchanged by LA/C KD. $n = 17$, 14, and 13 for WT, TSA, and LA/C KD, respectively. (B) Resistance to nuclear surface area change, E_{SA}, is unchanged by TSA but decreased by LA/C KD. $n = 17$, 14, and 13 for WT, TSA, and LA/C KD, respectively. (C) α, the exponent for $F_{\Delta NCSA}$, is unchanged by TSA and LA/C KD. $n = 16$, 14, and 13 for WT, TSA, and LA/C KD, respectively. (D) β, the exponent for $F_{\Delta NP}$, is unchanged by TSA and LA/C KD. $n = 16$, 14, and 11 for WT, TSA, and LA/C KD, respectively. (E) The difference in indentation at the onset of change in *NP* and *NCSA* is unchanged by TSA and LA/C KD. $n = 17$, 14, and 13 for WT, TSA, and LA/C KD, respectively. (F) The strain in *NP* at the transition point between regime 1 and regime 2 is unchanged by TSA and LA/C KD. $n = 16$, 14, and 11 for WT, TSA, and LA/C KD, respectively. Red bars represent mean and SEM. NS, not significant. *, $p < 0.05$.

Empirical model of nuclear deformation is independent of modifications to chromatin and lamin A/C

An alternative explanation for the decreases in E_V and E_{SA} seen upon TSA treatment and LA/C KD, respectively, is that our proposed empirical model (Eq. 1) is no longer valid after these treatments. More specifically, we could be observing changes in E_V and E_{SA} that are actually representative of changes in the scaling relationships between force and nuclear morphology themselves; that is, α and β could be dependent on chromatin compaction and lamin A/C expression. To address this explanation, we performed the analysis previously described to extract α and β from both the TSA-treated and the LA/C KD samples. We found no significant change in either α or β (Figure 3, C and D), meaning the previously determined scaling relationships between nuclear morphology and applied force are unchanged. Because these scaling relationships remain constant, our observed changes in E_V and E_{SA} are indicative of changes in the nucleus' ability to resist strain in nuclear volume and nuclear surface area.

Furthermore, we observed no significant difference in $\Delta\delta$ (Figure 3E) or the strain in *NP* at the transition point (Figure 3F). This implies that the existence of the strain-stiffening effect is more closely related to nuclear geometry and the manner of deformation than the relative stiffnesses associated with the volume and surface area of the nucleus. This result is supported by previous findings in micromanipulation studies (Banigan *et al.*, 2017). The lack of changes in scaling (α and β) and transition (indentation and strain) solidifies our conclusions regarding the role of chromatin and lamin A/C in separately resisting strain in nuclear volume and surface area, respectively.

Chromatin decompaction and lamin A/C KD separately regulate nuclear curvature under compression

Recent studies have connected nuclear curvature to locations of nuclear rupture and subsequent DNA damage. Through AFM compression with both 4.5-μm-diameter beaded cantilevers and sharp tip cantilevers (diameter < 0.1 μm), a correlation between indentation with high-curvature probes and nuclear rupture was reported (Xia *et al.*, 2018). Similarly, nuclear blebs induced by increases of euchromatin were shown to systematically form at the pole of the major axis, which is the site of highest curvature (Stephens *et al.*, 2018). We then sought to study the roles of chromatin and lamin A/C in nuclear curvature dynamics during AFM compression.

Nuclear curvature, defined as the inverse of the radius of a best-fit circle, was extracted for each point in the discretized perimeter of the nucleus for every image collected during the indentation. Before compression, the nucleus shows two peaks corresponding to the ends of the oval-shaped nucleus (Figure 4A). Once compressed, the nucleus shows a new, clearly defined peak at approximately 10 μm; this peak corresponds to the new curvature formed as a result of indentation with the AFM (Figure 4B and Supplemental Movie 2). By fitting a Gaussian curve to this peak for each frame in the indentation (Figure 4C), we can study how curvature changes as a function of indentation; specifically, we extract maximum curvature at the site of indentation. We observed that in the regime over which nuclear curvature changes, there is a linear relationship between maximum nuclear curvature and indentation (Figure 4D). Eventually the maximum nuclear curvature plateaus as it cannot exceed that of the AFM probe.

Maximum nuclear curvature was plotted against indentation and compared between perturbation and control wild-type (WT) nuclei (Figure 4, E–G). We discovered a significant decrease ($p < 0.01$ for a *t* test) between the mean slope of maximum curvature versus indentation for TSA-treated cells. This implies that larger indentations are necessary to induce that same of amount of nuclear curvature in TSA-treated cells as compared with WT cells. Contrary to chromatin

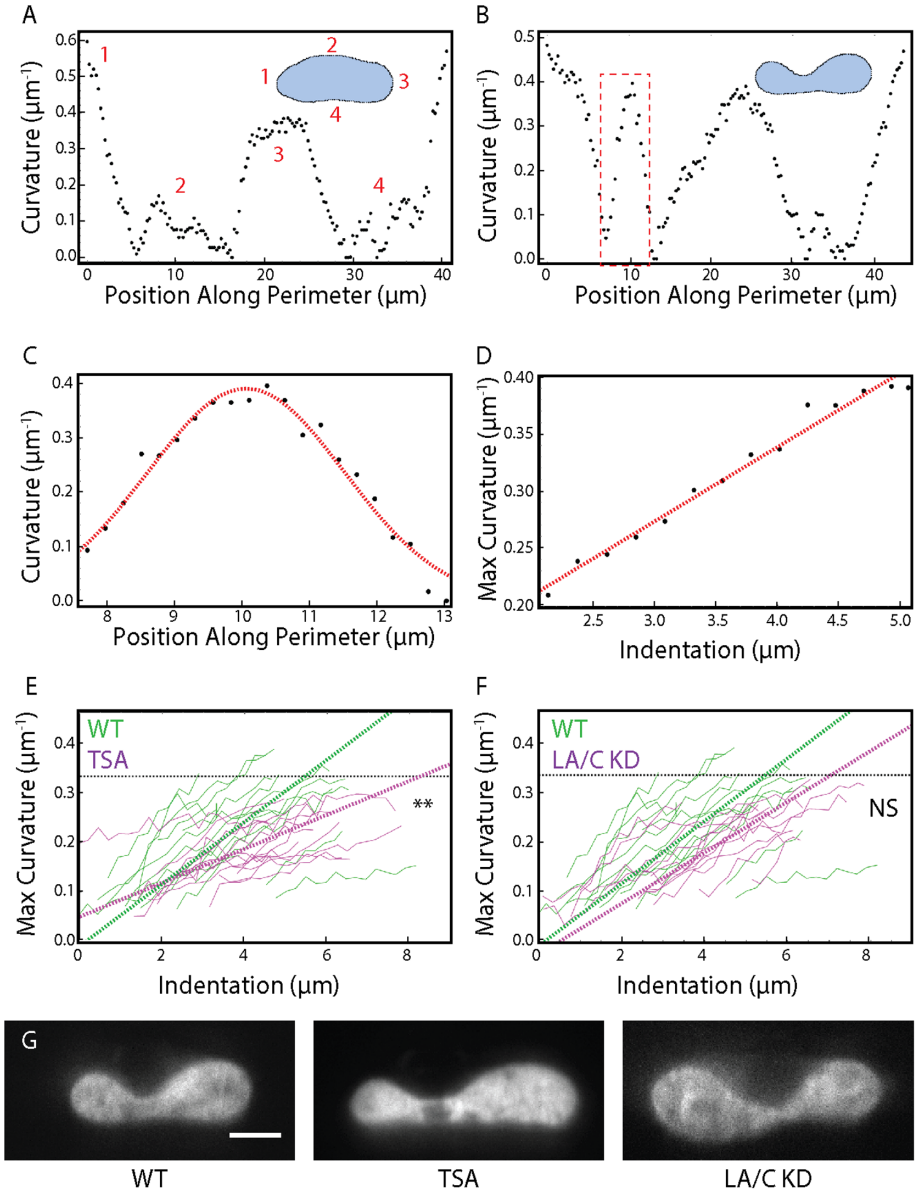

FIGURE 4: Dynamic nuclear curvature analysis during AFM indentation. (A) Nuclear curvature vs. position along perimeter for an undeformed nucleus. The inset displays the mask of the nucleus and the discretization of the perimeter. (B) Nuclear curvature vs. position along the perimeter for a deformed nucleus. The inset displays the mask of the nucleus and the discretization of the perimeter. Note the additional peak centered around 10 μm representing the site of indentation. (C) A Gaussian fit to the peak at the site of indentation extracts maximum curvature under the AFM bead (red dashed box in B). (D) Maximum curvature plotted during the entire indentation. A linear fit is performed for the region of changing curvature. (E) Maximum curvature as a function of indentation plotted for $n = 14$ WT cells and $n = 14$ TSA-treated cells. ** represnts $p < 0.01$ for a t test comparing the mean slope of maximum curvature vs. indentation. (F) Maximum curvature as a function of indentation plotted for $n = 14$ WT cells and $n = 13$ LA/C KD cells. Black dashed line represents curvature of the AFM bead. NS represents no significance for a t test comparing the mean slope of maximum curvature vs. indentation. (G) Representative images of SKOV3 nuclei (H2B) under maximum compression with various treatments. Scale bar = 5 μm.

decompacted cells, we observed no significant change in the mean slope of maximum curvature versus indentation for LA/C KD cells as compared with WT cells; this could be due to either a minimal contribution of lamin A/C to nuclear curvature or an inability to detect the changes in nuclear curvature due to the geometry of our assay or the degree of knockdown of lamin A/C. While not studied here, our ability to monitor the dynamics of nuclear curvature under compression will facilitate further studies of both varied deformation geometries and increased chromatin compaction and lamin A/C levels.

Two-material finite element model correlates resistances to morphology changes with material properties

To validate our conclusions and connect our results to mechanical properties, we developed a simple computational model of AFM indentation experiments. As the nucleus is the stiffest subcellular structure and the focus of our analysis, we chose to model only deformation of the nucleus. We constructed an axisymmetric FEA model featuring a stiff, spherical, polystyrene indenter and an ellipsoidal nucleus (Figure 5A and Supplemental Movie S3). Previous research has examined FEA models of AFM (Chen and Lu, 2012; Liu *et al.*, 2019), yet to our knowledge none have examined the relationship of nuclear morphology and force. The nucleus in our model features two separate materials: an infinitely thin, elastic membrane with a stretch modulus (γ) wrapped around an elastic solid with an elastic modulus (E). This then does not account for the interaction between the outer nuclear membrane and the endoplasmic reticulum, and instead models primarily the closed system of the nuclear lamina and chromatin. The model assumes quasistatic behavior.

We simulated AFM indentation with varied values of E and γ and examined the qualitative changes in the force-indentation curves (Figure 5B). We found that varying the elastic modulus leads to softening over the entirety of the indentation. However, variations in the stretch modulus of the elastic layer led to altered behavior only at larger indentations (>0.5 μm). This corresponds directly with our observation from our AFM-LS experiments. We showed that decondensation of chromatin and knockdown of lamin A/C lead to decreases in E_V and E_{SA}, respectively, and E_V provides resistance over the entire indentation while E_{SA} provides the additional resistance at larger indentations.

Observing the same qualitative behavior in the force-indentation curves provided motivation to correlate the material properties of the FEA model (E, γ) with E_V and E_{SA}. To do so, we performed identical analysis for extracting E_V and E_{SA} as previously described on our FEA model data. By varying either E or γ while keeping the other constant, we were able to study these correlations. We examined correlations between E_V (Figure 5C) and E_{SA} (Figure 5D) with E (blue) and γ

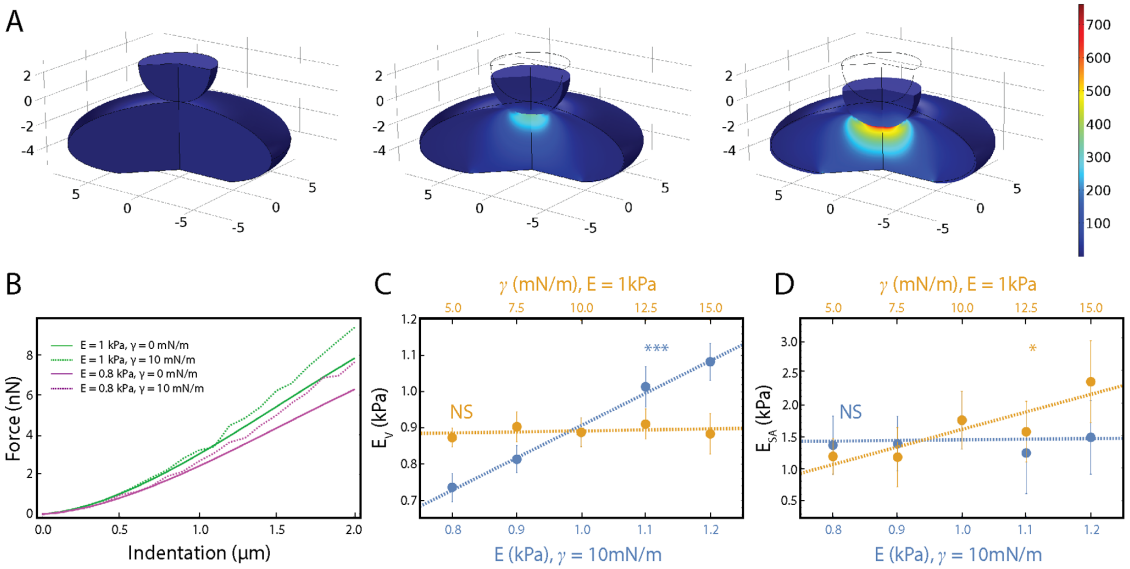

FIGURE 5: Finite element analysis (FEA) model of AFM indentation. (A) Selected frames from a FEA simulation of a nucleus under compression. The nucleus has an elastic modulus, E, and a separate stretch modulus, γ. (B) Force vs. indentation shown for varied E and γ. (C) Resistance to nuclear volume change, E_V, plotted against variations in both E and γ. A significant correlation ($p < 0.001$) is seen between E_V and E, but no significant correlation is seen between E_{SA} and E. (D). Resistance to nuclear surface area change, E_{SA}, plotted against variations in both E and γ. A significant correlation ($p < 0.05$) between E_{SA} and γ is seen, but no significant correlation is seen between E_{SA} and E.

(orange). We observed a significant, linear correlation between E_V and E as well as E_{SA} and γ; no significant correlation was observed between either E_V and γ or E_{SA} and E. This shows that our resistances to nuclear volume change and nuclear surface area change (E_V and E_{SA}) are indicative of material properties of the nucleus. Specifically, E_V is a representative measure of the elastic modulus of the nucleus and E_{SA} is a representative measure of the nuclear stretch modulus. We then find that our measured mean E_V of 0.58 kPa corresponds to $E = 0.63$ kPa and our measured mean E_{SA} of 0.79 kPa corresponds to $\gamma = 2.5$ mN/m, both of which are consistent with the current literature for Young's modulus measurements of the nucleus and stretch modulus of the nuclear membrane, respectively (Dahl *et al.*, 2004, 2005; Mazumder *et al.*, 2008; Schape *et al.*, 2009; Liu *et al.*, 2014; Neubert *et al.*, 2018; Wang *et al.*, 2018; Rosso *et al.*, 2019). Furthermore, we varied the size of our model nucleus and found that E_V and E_{SA} are independent of initial nuclear size (Supplemental Figure S8), similar to our results from experiments (Supplemental Figure S5).

DISCUSSION

Nuclear morphology provides an estimate of external forces

Our combined AFM-LS approach to studying nuclear mechanics first showed the existence of two regimes of deformation: one at low levels of indentation (regime 1) and one at high levels of indentation (regime 2). In regime 1, we observed only changes in nuclear volume; in regime 2, we observed changes in both nuclear volume and apparent surface area. This allowed us to extract scaling relationships between applied external forces and changes in nuclear morphology, leading to an empirical model of nuclear deformation characterized by two fitting parameters: E_V and E_{SA} (Figure 2). These fitting parameters provide a metric of resistance to nuclear volume change and nuclear surface area change, respectively, but further are directly proportional to the elastic modulus of the nucleus and the nuclear stretch modulus (Figure 5).

Often missing from current studies, are measurements of the external stress a nucleus experiences throughout a given experiment. Such measurements could provide additional context for interpreting why certain phenomena may be occurring. For example, constricted migration assays have allowed investigators to study how deficiencies in the nuclear lamina lead to increased migration rates (Shin *et al.*, 2013; Davidson *et al.*, 2014; Harada *et al.*, 2014), higher rates of nuclear rupture (Denais *et al.*, 2016), and increases in plastic damage (Harada *et al.*, 2014; Davidson *et al.*, 2015; Cao *et al.*, 2016), all of which are relevant for understanding disease states and cellular function. Our work provides a means of estimating the external force applied to a nucleus simply through measuring nuclear morphology in the plane of applied force. Clear limitations exist for applying this model, such as complex 3D nuclear strains; however, some common assays for studying nuclear dynamics could benefit from our model.

Chromatin and lamin A/C govern different forms of deformation

With our approach we were able to separate deformations of nuclear volume and nuclear surface area and tease apart how the mechanical constituents of the nucleus are responsible for each class of deformation. Specifically, we showed through disruption of histone–histone interactions via TSA treatment that chromatin resists strain in nuclear volume, but not in the nuclear surface area. We also showed through a knockdown of lamin A/C that the nuclear lamina resists strain in the nuclear surface area, but not in the nuclear volume. This further implies that chromatin dictates the mechanics of small indentations, whereas lamin A/C is relevant for large indentations. Additionally, through our FEA modeling we find that alterations in chromatin compaction and lamin A/C expression directly alter the nuclear elastic and stretch moduli, respectively. These findings are in agreement with work showing that stretching of isolated nuclei via micromanipulation with micropipettes yields a two-regime force response where chromatin regulates the low-deformation regime and

lamin A/C regulates the high-deformation regime (Stephens *et al.*, 2017). These results help to provide a guide for AFM experiments in that small indentation measurements will likely probe only the mechanical properties of the chromatin, and large indentation measurements will need additional compensation beyond standard contact mechanics models to account for stretching of the nuclear lamina.

Previous research has also shown that in micropipette aspiration studies, the mechanics of swollen nuclei are dominated by the nuclear lamina, whereas the mechanics of shrunken nuclei are governed in part by chromatin (Dahl *et al.*, 2005). This result that shifting the primary load-bearing structure from chromatin to the nuclear lamina via swelling is consistent with our results as swelling would prestretch the nuclear surface area, thus eliminating regime 1 entirely and leaving only the lamina-dominated regime 2. Studies of osmolarity have also shown similar phenomena that can be explained by our model. Cell volume and inverse osmolarity follow a linear relationship, which can be modeled by the Boyle Van't Hoff relation (Nobel, 1969). Nuclei, however, have been shown to deviate from this linear relationship at large swelling volumes. To match this behavior, an additional term modeling nuclear membrane tension that is proportional to the nuclear surface area must be added (Finan *et al.*, 2009), consistent with our findings.

AFM studies of mechanical properties have historically been used to study small-deformation mechanical properties because of the limitations of the analytical models applied to resulting data. Using cantilevers with large (10 μm) diameter beads positioned above the nucleus, force-indentation curves were collected on HT1080 fibrosarcoma cells for relatively low indentations (~1 μm). The Hertz model was fit to the force-indentation curves to extract an elastic modulus. They showed that TSA treatment resulted in nuclear softening (Krause *et al.*, 2013). This is consistent with our results showing that TSA treatment reduces E_V, which is the primary resistance at low indentations and proportional to the elastic modulus of the nucleus. A separate AFM study on isolated *Xenopus* oocytes revealed not only that increases in lamin A resulted in nuclear stiffening, but that the force-indentation curves become more linear as a function of lamin A expression levels (Schape *et al.*, 2009); a linear force-indentation curve is representative of a pressurized shell (Vella *et al.*, 2012). They were able to extract a nuclear membrane tension by fitting the end of the force-indentation curve to a linear relationship, and it is crucial to note that they indented nuclei up to approximately 10 μm. By fitting the end of the force-indentation curves for large indentations, they effectively extracted the mechanical properties of regime 2. Our results are then consistent in that we also showed a dependency of E_{SA} on lamin A/C expression; this implies that lower levels of lamin A/C reduce the nuclear stretch modulus at large nuclear deformations.

Our work provides a synthesis of these previous studies, helping to piece together separate results into a single, cohesive explanation for the force response of the nucleus. Previous AFM studies using Hertzian analysis could only observe when nuclei became softer or stiffer under a given treatment. That is, chromatin decondensation and lamin A/C knockdowns show an apparently identical softening response (decrease in elastic modulus) under Hertzian analysis (Krause et al., 2013; Rauschert *et al.*, 2017), despite having distinctly different roles in nuclear compression as shown here. With knowledge of both the length scales of deformation for which chromatin and lamin A/C are relevant as well as the specific morphological deformations against which they protect, we can progress forward to understanding their relative contributions in disease and function.

The role of nuclear curvature

We observed that chromatin decondensation through TSA treatment resulted in less nuclear curvature during indentation as compared with WT, whereas LA/C KD nuclei showed no change in curvature under compression in our assay. We hypothesize that this is due to a change in the relative resistances to nuclear volume and nuclear surface area strains that we have previously shown. By decreasing the bulk resistance, the energy necessary to deform the nuclear volume relative to the nuclear surface area decreases. Minimization of energy cost then implies that the nucleus will undergo larger volume changes and smaller surface area changes. Decreased nuclear curvature is one means by which the nucleus could accommodate larger volume changes with less stretching of the nuclear surface area. Our hypothesis for the decreased rate of curvature change in TSA-treated cells would lead us hypothesize that LA/C KD cells would show a higher rate of curvature change, or that overexpression of lamin A/C would mimic the behavior of TSA-treated nuclei. Our observation of no significant change could either be due to a lack of correlation between lamin A/C and nuclear curvature, or more likely due to the geometry of the AFM probe and minimal knockdown of lamin A/C levels limiting our ability to observe the effect LA/C KD would have on nuclear curvature. Regardless, the dependence of nuclear curvature on chromatin compaction levels clearly shows that the nucleus behaves as a two-material system. For a simple elastic solid—the curvature at the site of indentation is independent of the Young's modulus—a second material is necessary to observe altered deformation patterns by changing the material properties. This further confirms that both chromatin and lamin A/C contribute to nuclear stiffness in compression.

The relevance of nuclear curvature has primarily been linked to rupture of the nuclear envelope as well as development of nuclear blebs. Previous work has examined the correlation between nuclear curvature and nuclear envelope rupture through AFM (Xia *et al.*, 2018). U2OS cells were compressed with a constant force using both sharp (diameter < 0.1 μm) tips and 4.5-μm beads. Nuclear rupture was shown to be significantly more frequent when using the sharp tip as detected by mislocalization of YFP-NLS into the cytoplasm. Similarly, a constricted migration assay has revealed that it is rather the nuclear curvature, as opposed to tension, that is relevant for nuclear envelope rupture (Xia *et al.*, 2019). Nuclear blebs have also been shown to systematically form at sites of high curvature (Stephens *et al.*, 2018; Cho *et al.*, 2019) and are prone to rupture (Stephens *et al.*, 2019). Specifically, chromatin decompaction alone was sufficient to induce an increase in nuclear blebs (Stephens *et al.*, 2018). Nuclear curvature is then highly relevant for understanding the mechanical integrity of nuclei, as loss of nuclear compartmentalization due to rupture causes nuclear dysfunction that may contribute to human disease (Davidson and Lammerding, 2014; Stephens *et al.*, 2019). Our work suggests that lamin A/C may not be important for nuclear curvature. However, a valid alternate hypothesis is that the geometry of our bead limits our ability to detect the effect of the lamin A/C KD on nuclear curvature. We have clearly shown, however, that the state of compaction of chromatin has a direct link to the nuclear curvature, and we hypothesize that this is due to the altered, relative contributions of the nuclear elastic modulus and nuclear stretch modulus.

Our results regarding the dynamics of nuclear curvature under indentation also provide insight into how nuclear mechanotransduction may be altered through chromatin decompaction. We show that the nucleus develops less curvature during indentation for TSA-treated cells, simultaneously implying that there is less stretching of the nuclear envelope. As previously noted, stretching of the nuclear

lamina is thought to be a fundamental mechanism of nuclear mechnotransduction (Enyedi and Niethammer, 2017). The state of compaction of chromatin may then indirectly alter transcription or the function of stretch-activated channels (Donnaloja *et al.*, 2019) if the nucleus is undergoing external stress, as we have shown the distribution of strain to be dependent on chromatin compaction.

Nuclear morphology and function

Nuclear volume has been shown to be directly correlated with transcriptional activity. In one study, NIH3T3 mouse fibroblasts cultured on fibronectin-patterned coverslips were uniformly compressed with an additional weighted coverslip. This resulted both in an increase in chromatin condensation as well as a decrease in nuclear volume, both of which correlated with the subsequent reduction in transcriptional activity (Damodaran *et al.*, 2018). Separately, a migration assay has been used to show that transcription activity is altered as a result of introducing a constriction to the migration pathway (Jacobson *et al.*, 2018), which can decrease nuclear volume. Through showing chromatin is partially responsible for resisting nuclear volume strain and coupling this result with previous studies regarding nuclear volume and function, we conjecture that the mechanical properties of chromatin aid in regulating its own condensation and transcriptional activity. We further see that the nucleus is susceptible to volume changes at low levels of indentation, meaning these downstream effects of volume change can occur as a result of intracellular forces.

Stretching of the nuclear surface, however, has different implications for nuclear function and mechanotransduction (Enyedi and Niethammer, 2017). The nucleus is a mechanosensor that can convert mechanical signals at the cell surface into chemical responses (Kirby and Lammerding, 2018). This physical connection from integrins to the nucleus through the cytoskeleton, the LINC complex, and the nucleus was first shown by pulling fibronectin-coated micropipettes attached to the cell surface (Maniotis *et al.*, 1997). It was later shown that by twisting fibronectin-coated magnetic beads attached to the cell surface, one could induce stretching of chromatin and subsequent up-regulation of transcription activity (Tajik *et al.*, 2016). The distribution of stresses along the nuclear lamina is believed to be the primary mechanism responsible for such responses (Enyedi and Niethammer, 2017), which has led to the hypothesis of stretch activation along the nuclear envelope (Donnaloja *et al.*, 2019). By connecting expression levels of lamin A/C to resistances to change in nuclear surface area and consequently the nuclear stretch modulus, we have shown the relevance of lamin A/C to mechanoresponses governed by stretches in the nuclear envelope. Interestingly, we observe such nuclear surface area stretches only at large deformations. This implies that the nuclear lamina is relevant primarily for processes such as cellular migration or joint compression, and that the mechanoresponses associated with nuclear envelope stretches are not likely to happen outside of such processes that cause macroscopic, whole-cell deformations.

MATERIALS AND METHODS

Plasmid construction

LZ10 PBREBAC-H2BHalo was a gift from James Zhe Liu (HHMI Janelia Reseach Campus, Ashburn, VA; Addgene plasmid #91564; http://n2t.net/addgene:91564; RRID: Addgene_91564; Li *et al.*, 2016). pR-pre-EGFP was a gift from Sergio Grinstein (Hospital for Sick Children, Toronto, ON; Addgene plasmid #17274; http://n2t.net/addgene:17274; RRID: Addgene_17274; Yeung *et al.*, 2006). Piggybac plasmid PB513Bm2 was made by removing copGFP from PB513B-1 (System Biosciences) by PCR-based mutagenesis. PBREBAC_H2BHalo and PB513Bm2 encode the G418 and puromycin-resistant gene, respectively. The PB513Bm2_SNAP-KRas-tail vector was generated using PB513Bm2 as the backbone and SNAP_KRas-tail as the insert. Specifically, EGFP in pR-pre-EGFP was replaced with SNAP tag, then both pR-pre_SNAP_KRas-tail and PB513Bm2 were digested using *Nhe*I-HF and *Bam*H1-HF restriction enzymes (New England Biolab [NEB]). The products were purified using the QiaQUICK Gel Extraction Kit protocol (Qiagen) and then ligated together using T4 DNA ligase (NEB) according to the manufacturer's instructions. Prior to use, the plasmid sequences were confirmed by sequencing using the CMV-Forward primer at Genewiz (NJ).

Generation of SKOV3 cell line and cell culture

SKOV3 cells were obtained from ATCC (HTB-77) and maintained in DMEM (Corning; 15013CV) supplemented with 10% fetal bovine serum (FBS; Sigma-Aldrich) and 1% GlutaMAX (Life Technologies). SKOV3 cells coexpressing H2B-Halo and SNAP_KRas-tail were generated through two consecutive transfections. We first produced a stable SKOV3 cell line expressing H2B-Halo to label the nucleus and then used those cells to produce a stable cell line expressing SNAP_KRas-tail to label the plasma membrane. The transfection was performed using Fugene HD transfection reagent (Promega) according to the manufacturer's instructions. Briefly, SKOV3 cells were seeded onto a six-well plate at 5×10^4 cells per well, 24 h before transfection. For each well, we used 6 µl of Fugene HD transfection reagent, 3 µg piggyBac transgene plasmid (LZ10 PBREBAC_H2BHalo or PB513Bm2_SNAP_KRastail), and 0.6 µg of piggyBac transposase plasmid (ratio at 5:1). After 24 h transfection, the medium was replaced with the fresh culture medium and the cells were recovered for 24 h. Stable transfectants were selected by gradually increasing antibiotics concentrations: geneticin (G418) at a concentration to 1 mg/ml for PB-Halo-H2B and puromycin at a concentration to 2 µg/ml for PB513Bm2-SNAP-KRas-tail. SKOV3 cells were grown in DMEM F12 without phenol red (Life Technologies), 5% FBS (Sigma-Aldrich), and 1× antibiotic antimycotic (Life Technologies). On the day before experiments they were trypsinized and plated at low density on fibronectin-coated polyacrylamide gels. Janelia Fluor 549 and 503 (10 µl) was added 2 h before experiments, and washed out immediately before cells were examined. Janelia Fluor 503 was not used in lamin A/C KD cells as to not conflate the GFP reporter signal.

Production of polyacrylamide gels

Polyacrylamide gels were used as the cell substrate to eliminate reflections during side-view imaging. They were therefore produced to be at high stiffness (55 kPa), and relatively thin (10–30 µm thick). They were produced and coated with fibronectin by the methods described in our previous work (Nelsen *et al.*, 2019). Briefly, 10 µl of activated gel solution was deposited on (3-Aminopropyl)triethoxysilane (APTES)-treated 40-mm round coverslips, and a 22 × 22 mm square coverslip quickly placed on top. The top coverslip had been treated with hexamethyldisilazane (HMDS) via vapor deposition to facilitate easy removal after polymerization, and the gel included 1% polyacrylacrylic acid to provide carboxylic acid groups within the gel and promote adhesion to the APTES-coated glass substrate. After gelation and coverslip removal under deionized water, the gel was allowed to dry in a Biosafety hood, sufficiently to allow placement of a 10-mm-diameter glass cloning cylinder (316610; Corning) lightly coated with vacuum grease (1597418; Dow Corning). As soon as each cloning cylinder was placed, a solution of 10 mg/ml 1-ethyl-3-(3-dimethylaminopropyl) carbodiimide hydrochloride (EDAC) and 1 mg/ml N-Hydroxysuccinimide (NHS) in phosphate-buffered saline (PBS) was

placed into the cloning rings. The assembly was placed into sterile plastic Petri dishes. The dishes were then placed in a 37°C chamber at 100% humidity for 15 min. The EDAC buffer was then replaced twice with PBS at room temperature, and then with 10 μg/ml (1 μg/ml for rounded cell experiments) fibronectin for 30 min at 37°C. The fibronectin solution was replaced with PBS twice, and then with DMEM F12 growth media. Samples were finally placed in the cell culture incubator to equilibrate at least 30 min before cells are added.

Combined AFM and side-view light sheet microscopy

The intricate details of our AFM-LS system, both regarding the optical design and integration of the atomic force microscope, are described in our previous work (Liu *et al.*, 2019; Nelsen *et al.*, 2019). Beaded cantilevers (Figure 1C) were generated by first drying nominally 6-μm-diameter carboxylate beads onto a coverslip (17141-5; Polysciences); a small amount of UV-curable glue (NOA81; Norland Products) was spread onto the coverslip. A cantilever (Arrow TL1; Nanoworld) was mounted onto the AFM head (Ayslum Research MFP3D; Oxford Instruments), which was lowered over the aforementioned coverslip. Using the manual height adjustment on the AFM, the cantilever was lowered first into the glue and then overtop of a bead. A UV flashlight was used to cure the glue for 1 min; the cantilever was removed and set to cure for an additional 5 min. Once beaded, cantilevers were calibrated in media using the thermal tune method (Gavara, 2017); the nominal spring constant was 0.03 N/m.

Cells prepared as described above were placed onto the AFM-LS system in a custom, 3D-printed mount (uploaded as Thingiverse 2035546). Cells were kept in DMEM F12 with 15 mM HEPES without phenol red (Life Technologies) while on the microscope; this media is not CO_2 independent. An objective lens heater (Hk-100; Thorlabs) with a PIV controller (TC200, Thorlabs) and a heated scanning stage (900.062 MFP3D scanner; Oxford Instruments) were used to keep the sample at 37°C. Samples were kept on the AFM-LS system for no more than a couple of hours to ensure viability; cells were observed to be viable throughout all experiments. The AFM headed with a calibrated cantilever was placed atop the sample and the cantilever was lowered over a cell of interest. Side-view imaging is achieved by placing a small (180-μm) mirror (8531-607-1; Precision Optics) adjacent to a cell of interest and raising the objective lens (UplanSAPO 60×/1.2 W; Olympus) until the image plane intersects the mirror. Details regarding mirror alignment and production are given in our previous work (Nelsen *et al.*, 2019). With the AFM in place, the mirror is placed next to the cell of interest such that the cantilever sits between the mirror and the cell. A vertical light sheet propagates out of the objective lens and an electrically tunable lens (ETL) was used to ensure the waist of the light sheet was in the cell. A second ETL is used in the detection path to dynamically adjust focus without moving the objective lens (Liu *et al.*, 2019).

Force curves were taken at a loading rate of 1 μm/s unless otherwise stated. The trigger point for the *z*-piezo movement was set such that the nucleus was compressed to approximately 2 μm. The *z*-piezo was then fixed in a closed-loop feedback mode for 60 s, after which the AFM retraced and continued recording data for an additional 15 s. Data from the AFM was recorded at a bandwidth of 2 kHz. A square wave from the AFM was sent to a DAQ board (PCIe-6323; National Instruments) that was used to synchronize both the camera (ORCAFlash4.0 V3; Hamamatsu) and laser light (OBIS-561-150-LS and OBIS-488-150-LS; Edmund Optics). Unless otherwise stated, each channel (488 nm and 561 nm) had an exposure time of 100 ms, and 25 ms was taken between each frame resulting in a two-color frame acquisition rate of 4 Hz. Custom software was designed for the synchronization process and image acquisition.

Nuclear morphology extraction and curvature analysis

All nuclear morphology extraction was performed in FIJI (Schindelin *et al.*, 2012) using side-view fluorescence images of H2B. A rolling-ball background subtraction was performed with a radius dependent on the size of the nucleus (~50–150 pixels). A Gaussian blur was then performed with a kernel size of 2 pixels based upon the full-width half maxmum (FWHM) of the system's point spread function (PSF). The FeatureJ Edges plugin (http://imagescience.org/meijering/software/featurej/) was used to determine the outline of the nucleus during compression; this outline was thresholded to generate a binary image. The binary outline was then dilated several pixels (2–5 pixels, depending on the initial image quality) to form a continuous boundary, after which the boundary was filled to generate a mask. The mask was eroded by the same amount as the initial dilation to form the final mask of the nucleus. FIJI's "analyze particles" feature was used to extract the cross-sectional area and perimeter of the nucleus throughout the AFM compression.

All curvature analysis was performed in Mathematica 11.2 (https://github.com/alihashmiii/curvatureMeasure). Masks of nuclei were imported and the mask boundary was discretized such that each discrete point was separated from the next by approximately 250 nm based upon the FWHM of the PSF of our system. For each point on the perimeter, a circle was fit to that point and the adjacent points within one-fourth of the circumference of the AFM bead on either side. Curvature was defined to be the inverse of the radius of the fitted circle; a curvature of 0 represents a flat line. To dynamically track the maximum curvature at the site of indentation, a Gaussian curve was fit to the curvature versus boundary point data in the region where the nucleus was indented.

Treatments of SKOV3 cells

For treatment with TSA, TSA was dissolved to 10 mM in dimethyl sulfoxide (DMSO), and then serially diluted in PBS to 4 μM on the day of treatment. A 4 μM solution (10 μl) of in PBS was then added to 190 μl of media in 10-mm cloning cylinders, for a final concentration of 200 nM. Experiments were carried out 24–28 h after drug addition. The 2×10^{-5} dilution of DMSO, giving 0.002% vol/vol final concentration, was judged to be insignificant to the TSA effect. A full description of our knockdown of lamin A/C is available in our previous work (Stephens *et al.*, 2017) Briefly, DNA for the interfering RNA was transfected using Fugene HD. The media was changed regularly after the first 2-d treatment. Cells were plated on days 3, 4, and 5, and used on days 4, 5, and 6, respectively. Two cells were excluded from the lamin A/C sample because they showed severe plastic damage, a phenomenon previously observed in the literature (Pajerowski *et al.*, 2007; Cao *et al.*, 2016) but not present in any other cell of the study (Supplemental Figure S9).

Immunofluorescence

To test whether the TSA treatment was effective at inhibiting histone deactylation, we plated cells as described and treated half with TSA as described, and half with a sham pipetting of PBS. At 24 h, cells were fixed in 4% formaldehyde, permeabilized with 0.25% Triton X-100, washed, and incubated with rabbit monoclonal antibody to acetyl histone H3 (Acetyl-Histone H3 (Lys9) (C5B11) Rabbit mAb #9649; Cell Signaling Technology), 1/400 dilution with 1 mg/ml bovine serum albumin as blocker, overnight. After primary antibody incubation, cells were washed three times, and incubated with Alexa Fluor 488 goat anti-rabbit IgG (Invitrogen), and 1/1000 dilution of Hoechst 33342 DNA stain for 1 h. After washing, cells were imaged at 150 ms exposure with 405 nm and 488 nm excitation light (objective lens: Plan Apo 60×/1.20 W; Nikon; Supplemental Figure S6, A and B).

To test whether the knockdown was successful, we fixed and stained parallel samples with lamin A/C antibody (E-1; sc-376248; Santa Cruz Biotechnology) as described above, but used a goat anti-mouse secondary antibody (Alexa Fluor 568; Invitrogen). Cells plated in parallel were stained with the same solutions and were imaged at 100 ms exposure with 488 nm and 568 nm excitation light (objective lens: UPlanFL N 40×/1.3 oil; Olympus; Supplemental Figure S7A).

After the collection of immunofluorescence images, nuclei were manually segmented in FIJI (Schindelin *et al.*, 2012). For the TSA verification, the mean intensity of the H3K9ac marker was calculated for all nuclei ($n = 43$ for WT, $n = 41$ for TSA). A *t* test shows a significant relative increase in H3K9ac of approximately 250% for TSA-treated cells as compared with WT cells (Supplemental Figure S6C). For the lamin A/C KD verification, the mean intensity of lamin was quantified for cells expressing the GFP reporter in LA/C KD nuclei ($n = 27$) and for all WT nuclei ($n = 58$). A *t* test shows a significant relative reduction in lamin expression for LA/C KD nuclei of approximately 40% as compared with WT nuclei (Supplemental Figure S7B). Note that LA/C KD nuclei appear to have a slightly larger spread area as compared with WT nuclei, which is consistent with previous findings (Kim *et al.*, 2018).

FEA

All FEA modeling was performed in COMSOL Multiphysics 5.2a (the full model is available upon request). The geometry was defined in 2D under axisymmetric assumptions. The AFM tip was modeled to be an elastic sphere of radius 3 μm with an elastic modulus of 3.5 GPa and Poisson ratio of 0.3. The nucleus was modeled to be an elastic ellipsoid with a long axis radius of 8.5 μm and a short axis radius of 3 μm. The bottom 1.5 μm of the ellipsoid was truncated and set to be a fixed constraint. The nucleus had a Poisson ratio of 0.3 and an elastic modulus varied about 1 kPa. The nucleus was wrapped in a thin elastic layer governed by a total spring constant, which varied about 10 mN/m. The thin elastic layer also changes the boundary condition between the nucleus and AFM tip such that forces on either side of the boundary are equal in magnitude and opposite in direction, but the displacements on either side of the boundary are no longer coupled. To simulate indentation, the AFM tip was incrementally stepped a total distance of 2 μm in steps of 0.1 μm. At each step, the MUMPS solver was used to solve for the displacement and stress along the mesh. A surface integral on the AFM tip provided the reactionary force at each indentation step; nuclear morphology was also extracted at each indentation step. All analyses were performed under that assumption of quasistatic behavior; that is, no time dependence was accounted for in our FEA model. The equation governing the behavior of elastic solids is given by

$$0 = \nabla \cdot \mathbf{S} + \overrightarrow{F_V} \tag{2}$$

where $\boldsymbol{S}$ is the stress tensor and $\vec{F}_v$ is the volume force. The equation governing the thin elastic layer is given by

$$\boldsymbol{S} \cdot \vec{n} = -\frac{\gamma}{A}\vec{u} \tag{3}$$

where $\boldsymbol{S}$ is the stress tensor, $\vec{n}$ is the vector normal to the surface, γ is the stretch modulus, A is the contact area, and $\vec{u}$ is the displacement field.

ACKNOWLEDGMENTS

We thank the Goldman Lab (Northwestern University Feinberg School of Medicine) for providing us with the siRNA plasmid to knockdown lamin A/C levels. We would also like to thank Jake Brooks for his help acquiring the scanning electron microscope image of the AFM cantilever. Finally, we want to thank the editor and reviewers for their thorough comments and suggestions that have improved the quality of this paper. C.M.H. is supported by the National Science Foundation (NSF) GRFP (DGE-1650116) and the Caroline H. and Thomas Royster Fellowship. M.K. is supported by National Institutes of Health (NIH) Grant no. 5T32GM-008570-19. A.D.S. is supported by Pathway to Independence Award NIHGMS K99GM-123195. E.T.O., M.R.F., and S.R. are supported by NIH and NSF (NSF/NIGMS 1361375) as well as NIH (NIBIB P41-EB002025).

REFERENCES

Balakrishnan S, Mathad SS, Sharma G, Raju SR, Reddy UB, Das S, Anantha-suresh GK (2019). A nondimensional model reveals alterations in nuclear mechanics upon hepatitis C virus replication. Biophys J 116, 1328–1339.

Banigan EJ, Stephens AD, Marko JF (2017). Mechanics and buckling of biopolymeric shells and cell nuclei. Biophys J 113, 1654–1663.

Beicker K, O'Brien ET 3rd, Falvo MR, Superfine R (2018). Vertical light sheet enhanced side-view imaging for AFM cell mechanics studies. Sci Rep 8, 1504.

Butin-Israeli V, Adam SA, Goldman AE, Goldman RD (2012). Nuclear lamin functions and disease. Trends Genet 28, 464–471.

Buxboim A, Irianto J, Swift J, Athirasala A, Shin JW, Rehfeldt F, Discher DE (2017). Coordinated increase of nuclear tension and lamin-A with matrix stiffness outcompetes lamin-B receptor that favors soft tissue phenotypes. Mol Biol Cell 28, 3333–3348.

Caille N, Thoumine O, Tardy Y, Meister JJ (2002). Contribution of the nucleus to the mechanical properties of endothelial cells. J Biomech 35, 177–187.

Cao X, Moeendarbary E, Isermann P, Davidson PM, Wang X, Chen MB, Burkart AK, Lammerding J, Kamm RD, Shenoy VB (2016). A chemo-mechanical model for nuclear morphology and stresses during cell transendothelial migration. Biophys J 111, 1541–1552.

Chen J, Lu G (2012). Finite element modelling of nanoindentation based methods for mechanical properties of cells. J Biomech 45, 2810–2816.

Cho S, Vashisth M, Abbas A, Majkut S, Vogel K, Xia Y, Ivanovska IL, Irianto J, Tewari M, Zhu K, *et al.* (2019). Mechanosensing by the lamina protects against nuclear rupture, DNA damage, and cell-cycle arrest. Dev Cell 49, 920–935.e5.

Chu FY, Haley SC, Zidovska A (2017). On the origin of shape fluctuations of the cell nucleus. Proc Natl Acad Sci USA 114, 10338–10343.

Dahl KN, Engler AJ, Pajerowski JD, Discher DE (2005). Power-law rheology of isolated nuclei with deformation mapping of nuclear substructures. Biophys J 89, 2855–2864.

Dahl KN, Kahn SM, Wilson KL, Discher DE (2004). The nuclear envelope lamina network has elasticity and a compressibility limit suggestive of a molecular shock absorber. J Cell Sci 117, 4779–4786.

Dahl KN, Scaffidi P, Islam MF, Yodh AG, Wilson KL, Misteli T (2006). Distinct structural and mechanical properties of the nuclear lamina in Hutchinson-Gilford progeria syndrome. Proc Natl Acad Sci USA 103, 10271–10276.

Damodaran K, Venkatachalapathy S, Alisafaei F, Radhakrishnan AV, Sharma Jokhun D, Shenoy VB, Shivashankar GV (2018). Compressive force induces reversible chromatin condensation and cell geometry dependent transcriptional response. Mol Biol Cell 29, 3039–3051.

Davidson PM, Denais C, Bakshi MC, Lammerding J (2014). Nuclear deformability constitutes a rate-limiting step during cell migration in 3-D environments. Cell Mol Bioeng 7, 293–306.

Davidson PM, Lammerding J (2014). Broken nuclei—lamins, nuclear mechanics, and disease. Trends Cell Biol 24, 247–256.

Davidson PM, Sliz J, Isermann P, Denais C, Lammerding J (2015). Design of a microfluidic device to quantify dynamic intra-nuclear deformation during cell migration through confining environments. Integr Biol (Camb) 7, 1534–1546.

Denais CM, Gilbert RM, Isermann P, McGregor AL, te Lindert M, Weigelin B, Davidson PM, Friedl P, Wolf K, Lammerding J (2016). Nuclear envelope rupture and repair during cancer cell migration. Science 352, 353–358.

De Sandre-Giovannoli A, Bernard R, Cau P, Navarro C, Amiel J, Boccaccio I, Lyonnet S, Stewart CL, Munnich A, Le Merrer M, Levy N (2003). Lamin A truncation in Hutchinson-Gilford progeria. Science 300, 2055.

Dimitriadis EK, Horkay F, Maresca J, Kachar B, Chadwick RS (2002). Determination of elastic moduli of thin layers of soft material using the atomic force microscope. Biophys J 82, 2798–2810.

Donnaloja F, Jacchetti E, Soncini M, Raimondi MT (2019). Mechanosensing at the nuclear envelope by nuclear pore complex stretch activation and its effect in physiology and pathology. Front Physiol 10, 896.
Enyedi B, Niethammer P (2017). Nuclear membrane stretch and its role in mechanotransduction. Nucleus 8, 156–161.
Erdel F, Baum M, Rippe K (2015). The viscoelastic properties of chromatin and the nucleoplasm revealed by scale-dependent protein mobility. J. Phys.: Condens. Matter 27, 064115.
Finan JD, Chalut KJ, Wax A, Guilak F (2009). Nonlinear osmotic properties of the cell nucleus. Ann Biomed Eng 37, 477–491.
Finan JD, Leddy HA, Guilak F (2011). Osmotic stress alters chromatin condensation and nucleocytoplasmic transport. Biochem Biophys Res Commun 408, 230–235.
Gavara N (2017). A beginner's guide to atomic force microscopy probing for cell mechanics. Microsc Res Tech 80, 75–84.
Haase K, Macadangdang JKL, Edrington CH, Cuerrier CM, Hadjiantoniou S, Harden JL, Skerjanc IS, Pelling AE (2016). Extracellular forces cause the nucleus to deform in a highly controlled anisotropic manner. Sci Rep 6, 21300.
Hanson L, Zhao WT, Lou HY, Lin ZC, Lee SW, Chowdary P, Cui Y, Cui BX (2015). Vertical nanopillars for in situ probing of nuclear mechanics in adherent cells. Nat Nanotechnol 10, 554-U92.
Harada T, Swift J, Irianto J, Shin JW, Spinler KR, Athirasala A, Diegmiller R, Dingal PC, Ivanovska IL, Discher DE (2014). Nuclear lamin stiffness is a barrier to 3D migration, but softness can limit survival. J Cell Biol 204, 669–682.
Hatch EM, Hetzer MW (2016). Nuclear envelope rupture is induced by actin-based nucleus confinement. J Cell Biol 215, 27–36.
Jacobson EC, Perry JK, Long DS, Olins AL, Olins DE, Wright BE, Vickers MH, O'Sullivan JM (2018). Migration through a small pore disrupts inactive chromatin organization in neutrophil-like cells. BMC Biol 16, 142.
Johnson KL (1985). Contact Mechanics, New York:Cambridge University Press.
Karcher H, Lammerding J, Huang H, Lee RT, Kamm RD, Kaazempur-Mofrad MR (2003). A three-dimensional viscoelastic model for cell deformation with experimental verification. Biophys J 85, 3336–3349.
Katiyar A, Tocco VJ, Li Y, Aggarwal V, Tamashunas AC, Dickinson RB, Lele TP (2019). Nuclear size changes caused by local motion of cell boundaries unfold the nuclear lamina and dilate chromatin and intranuclear bodies. Soft Matter 15, 9310–9317.
Khatau SB, Hale CM, Stewart-Hutchinson PJ, Patel MS, Stewart CL, Searson PC, Hodzic D, Wirtz D (2009). A perinuclear actin cap regulates nuclear shape. Proc Natl Acad Sci USA 106, 19017–19022.
Kim DH, Li B, Si FW, Phillip JM, Wirtz D, Sun SX (2015). Volume regulation and shape bifurcation in the cell nucleus. J Cell Sci 128, 3375–3385.
Kim JK, Louhghalam A, Lee G, Schafer BW, Wirtz D, Kim DH (2018). Nuclear lamin A/C harnesses the perinuclear apical actin cables to protect nuclear morphology (vol 8, 2017). Nat Commun 9, 1115.
Kirby TJ, Lammerding J (2018). Emerging views of the nucleus as a cellular mechanosensor. Nat Cell Biol 20, 373–381.
Krause M, te Riet J, Wolf K (2013). Probing the compressibility of tumor cell nuclei by combined atomic force-confocal microscopy. Phys Biol 10, 065002.
Lammerding J, Fong LG, Ji JY, Reue K, Stewart CL, Young SG, Lee RT (2006). Lamins A and C but not lamin B1 regulate nuclear mechanics. J Biol Chem 281, 25768–25780.
Lammerding J, Hsiao J, Schulze PC, Kozlov S, Stewart CL, Lee RT (2005). Abnormal nuclear shape and impaired mechanotransduction in emerin-deficient cells. J Cell Biol 170, 781–791.
Lammerding J, Schulze PC, Takahashi T, Kozlov S, Sullivan T, Kamm RD, Stewart CL, Lee RT (2004). Lamin A/C deficiency causes defective nuclear mechanics and mechanotransduction. J Clin Invest 113, 370–378.
Lammerding J, Wolf K (2016). Nuclear envelope rupture: actin fibers are putting the squeeze on the nucleus. J Cell Biol 215, 5–8.
Lee JSH, Hale CM, Panorchan P, Khatau SB, George JP, Tseng Y, Stewart CL, Hodzic D, Wirtz D (2007). Nuclear lamin A/C deficiency induces defects in cell mechanics, polarization, and migration. Biophys J 93, 2542–2552.
Lherbette M, dos Santos A, Hari-Gupta Y, Fili N, Toseland CP, Schaap IAT (2017). Atomic force microscopy micro-rheology reveals large structural inhomogeneities in single cellnuclei. Sci Rep 7, 8116.
Li L, Liu H, Dong P, Li D, Legant WR, Grimm JB, Lavis LD, Betzig E, Tijan R, Liu Z (2016). Real-time imaging of Huntingtin aggregates diverting target search and gene transcription. Elife 5, e17056.
Liu B, Hobson CM, Pimenta FM, Nelsen E, Hsiao J, O'Brien T, Falvo MR, Hahn KM, Superfine R (2019). VIEW-MOD: a versatile illumination engine with a modular optical design for fluorescence microscopy. Opt Express 27, 19950–19972.
Liu Y, Mollaeian K, Ren J (2019). Finite element modeling of living cells for AFM indentation-based biomechanical characterization. Micron 116, 108–115.
Liu HJ, Wen J, Xiao Y, Liu J, Hopyan S, Radisic M, Simmons CA, Sun Y (2014). In situ mechanical characterization of the cell nucleus by atomic force microscopy. ACS Nano 8, 3821–3828.
Maniotis AJ, Chen CS, Ingber DE (1997). Demonstration of mechanical connections between integrins, cytoskeletal filaments, and nucleoplasm that stabilize nuclear structure. Proc Natl Acad Sci USA 94, 849–854.
Mattaj IW (2004). Sorting out the nuclear envelope from the endoplasmic reticulum. Nat Rev Mol Cell Biol 5, 65–69.
Mazumder A, Roopa T, Basu A, Mahadevan L, Shivashankar GV (2008). Dynamics of chromatin decondensation reveals the structural integrity of a mechanically prestressed nucleus. Biophys J 95, 3028–3035.
Neelam S, Chancellor TJ, Li Y, Nickerson JA, Roux KJ, Dickinson RB, Lele TP (2015). Direct force probe reveals the mechanics of nuclear homeostasis in the mammalian cell. Proc Natl Acad Sci USA 112, 5720–5725.
Nelsen E, Hobson CM, Kern ME, Hsiao JP, O'Brien ET, Watanabe T, Condon BM, Boyce M, Grinstein S, Hahn KM, *et al.* (2019). Combined atomic force microscope and volumetric light sheet system for mechanobiology. BioRxiv, DOI: 10.1101/812396.
Neubert E, Meyer D, Rocca F, Gunay G, Kwaczala-Tessmann A, Grandke J, Senger-Sander S, Geisler C, Egner A, Schon MP, *et al.* (2018). Chromatin swelling drives neutrophil extracellular trap release. Nat Commun 9, 3767.
Nobel PS (1969). Boyle-Van't Hoff relation. J Theor Biol 23, 375–379.
Pajerowski JD, Dahl KN, Zhong FL, Sammak PJ, Discher DE (2007). Physical plasticity of the nucleus in stem cell differentiation. Proc Natl Acad Sci USA 104, 15619–15624.
Patteson AE, Vahabikashi A, Pogoda K, Adam SA, Mandal K, Kittisopikul M, Sivagurunathan S, Goldman A, Goldman RD, Janmey PA (2019). Vimentin protects cells against nuclear rupture and DNA damage during migration. J Cell Biol 218, 4079–4092.
Rauschert I, Aldunate F, Preussner J, Arocena-Sutz M, Peraza V, Looso M, Benech JC, Agrelo R (2017). Promoter hypermethylation as a mechanism for Lamin A/C silencing in a subset of neuroblastoma cells. PLoS One 12, e0175953.
Rosso G, Liashkovich I, Shahin V (2019). In situ investigation of interrelationships between morphology and biomechanics of endothelial and glial cells and their nuclei. Adv Sci (Weinh) 6, 1801638.
Schape J, Prausse S, Radmacher M, Stick R (2009). Influence of Lamin A on the mechanical properties of amphibian oocyte nuclei measured by atomic force microscopy. Biophys J 96, 4319–4325.
Schindelin J, Arganda-Carreras I, Frise E, Kaynig V, Longair M, Pietzsch T, Preibisch S, Rueden C, Saalfeld S, Schmid B, *et al.* (2012). Fiji: an open-source platform for biological-image analysis. Nat Methods 9, 676–682.
Schreiner SM, Koo PK, Zhao Y, Mochrie SG, King MC (2015). The tethering of chromatin to the nuclear envelope supports nuclear mechanics. Nat Commun 6, 7159.
Sen S, Subramanian S, Discher DE (2005). Indentation and adhesive probing of a cell membrane with AFM: theoretical model and experiments. Biophys J 89, 3203–3213.
Shimamoto Y, Tamura S, Masumoto H, Maeshima K (2017). Nucleosome-nucleosome interactions via histone tails and linker DNA regulate nuclear rigidity. Mol Biol Cell 28, 1580–1589.
Shin JW, Spinler KR, Swift J, Chasis JA, Mohandas N, Discher DE (2013). Lamins regulate cell trafficking and lineage maturation of adult human hematopoietic cells. Proc Natl Acad Sci USA 110, 18892–18897.
Stephens AD, Banigan EJ, Adam SA, Goldman RD, Marko JF (2017). Chromatin and lamin A determine two different mechanical response regimes of the cell nucleus. Mol Biol Cell 28, 1984–1996.
Stephens AD, Banigan EJ, Marko JF (2019). Chromatin's physical properties shape the nucleus and its functions. Curr Opin Cell Biol 58, 76–84.
Stephens AD, Liu PZ, Banigan EJ, Almassalha LM, Backman V, Adam SA, Goldman RD, Marko JF (2018). Chromatin histone modifications and rigidity affect nuclear morphology independent of lamins. Mol Biol Cell 29, 220–233.
Stephens AD, Liu PZ, Kandula V, Chen H, Almassalha LM, Herman C, Backman V, O'Halloran T, Adam SA, Goldman RD, *et al.* (2019). Physicochemical mechanotransduction alters nuclear shape and mechanics via heterochromatin formation. Mol Biol Cell 30, 2320–2330.
Swift J, Ivanovska IL, Buxboim A, Harada T, Dingal PC, Pinter J, Pajerowski JD, Spinler KR, Shin JW, Tewari M, *et al.* (2013). Nuclear lamin-A scales with tissue stiffness and enhances matrix-directed differentiation. Science 341, 1240104.

Tajik A, Zhang Y, Wei F, Sun J, Jia Q, Zhou W, Singh R, Khanna N, Belmont AS, Wang N (2016). Transcription upregulation via force-induced direct stretching of chromatin. Nat Mater 15, 1287–1296.

Tocco VJ, Li Y, Christopher KG, Matthews JH, Aggarwal V, Paschall L, Luesch H, Licht JD, Dickinson RB, Lele TP (2018). The nucleus is irreversibly shaped by motion of cell boundaries in cancer and non-cancer cells. J Cell Physiol 233, 1446–1454.

Toth KF, Knoch TA, Wachsmuth M, Frank-Stohr M, Stohr M, Bacher CP, Muller G, Rippe K (2004). Trichostatin A-induced histone acetylation causes decondensation of interphase chromatin. J Cell Sci 117, 4277–4287.

Vaziri A, Mofrad MRK (2007). Mechanics and deformation of the nucleus in micropipette aspiration experiment. J Biomech 40, 2053–2062.

Vella D, Ajdari A, Vaziri A, Boudaoud A (2012). The indentation of pressurized elastic shells: from polymeric capsules to yeast cells. J R Soc Interface 9, 448–455.

Wang X, Liu HJ, Zhu M, Cao CH, Xu ZS, Tsatskis Y, Lau K, Kuok C, Filleter T, McNeill H, *et al.* (2018). Mechanical stability of the cell nucleus—roles played by the cytoskeleton in nuclear deformation and strain recovery. J Cell Sci 131, 209627.

Xia Y, Ivanovska IL, Zhu K, Smith L, Irianto J, Pfeifer CR, Alvey CM, Ji J, Liu D, Cho S, *et al.* (2018). Nuclear rupture at sites of high curvature compromises retention of DNA repair factors. J Cell Biol 217, 3796–3808.

Xia Y, Pfeifer CR, Zhu K, Irianto J, Liu D, Pannell K, Chen EJ, Dooling LJ, Tobin MP, Wang M, *et al.* (2019). Rescue of DNA damage after constricted migration reveals a mechano-regulated threshold for cell cycle. J Cell Biol.

Yeung T, Terebiznik M, Yu LM, Silvius J, Abidi WM, Philips M, Levine T, Kapus A, Grinstein S (2006). Receptor activation alters inner surface potential during phagocytosis. Science 313, 347–351.

Zhang Q, Tamashunas AC, Agrawal A, Torbati M, Katiyar A, Dickinson RB, Lammerding J, Lele TP (2019). Local, transient tensile stress on the nuclear membrane causes membrane rupture. Mol Biol Cell 30, 899–906.